nature materials

Article

https://doi.org/10.1038/s41563-022-01414-y

Topological steering of light by nematic vortices and analogy to cosmic strings

Cuiling Meng[1,5], Jin-Sheng Wu[1,5] & Ivan I. Smalyukh[1,2,3,4]

Liquid crystals are widely known for their technological uses in displays, electro-optics, photonics and nonlinear optics, but these applications typically rely on de ning and switching non-topological spatial patterns of the optical axis. Here, we demonstrate how a liquid crystal's optical axis patterns with singular vortex lines can robustly steer beams of light. External stimuli, including an electric eld and light itself, allow us to recon gure these un5(sin Sl).5(aight –mtt)10(erninc)10(10000038(,e)10(at)-5(trons .).5(aP30.,

https://doi.org/10.1038/s41563-022-01414-y

as revealed for defects with $k = 3, 4, 6$ and 9 and their dimers (Extended Data Figs. 4 and 5). By shifting beams relative to these vortices, light trajectories can be dynamically reconfigured (Supplementary Video 2).

Experimental trajectories of optical solitons in LCs are fully reproduced by two different types of modelling (Fig. 1, Extended Data

https://doi.org/10.1038/s41563-022-01414-y

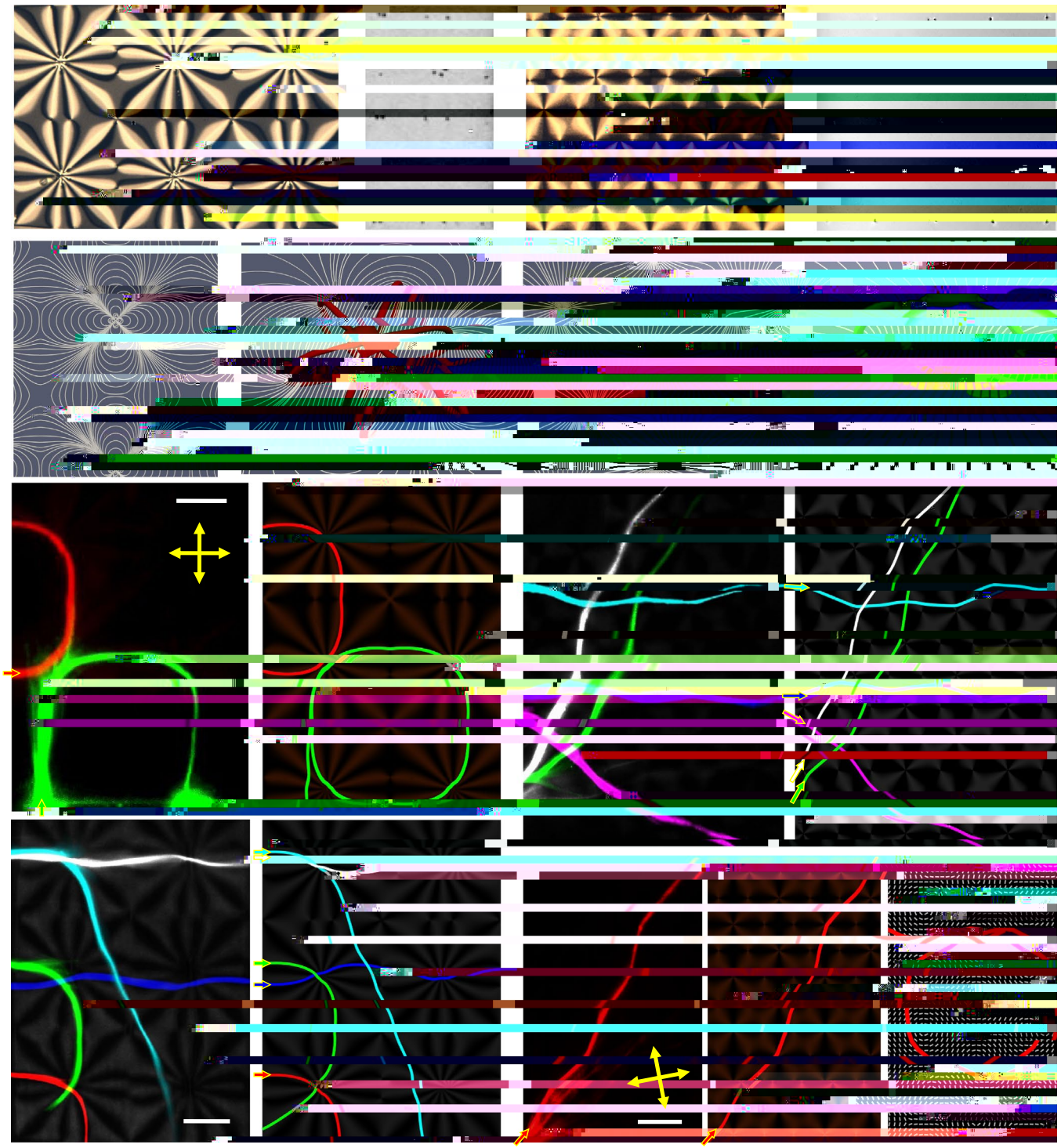

and compensated by $k = -1/2$ vortices, also cause beam meandering and deflection (Fig. 3m–q). Different from the $k = 3$ defects, however, light localization can occur only at large values of optical anisotropy of ~0.36 (Methods and Fig. 3q), which is accessible in LCs. Optical solitons traverse the sample with distinct light-steering vortices in a manner consistent with model predictions (Fig. 3m–p). Despite the common existence of many possible paths for a beam of finite width (Supplementary Video 6), we also observe single solitonic trajectories (Fig. 3o). Such interactions generate different soliton morphologies, including lightning-like and zigzag-like trajectories. Even slight changes of the entry locations of the optical solitons yield a dramatic, fascinating evolution of light steering by this vortex array (Supplementary Videos 5 and 6).

The scalar orientational order parameter is reduced within the

the range $\theta = 21.7–24°$, depending on the wavelength for which the Δn and n_e values are used. This matches the θ experimentally measured at distances much larger than the shortest vortex-beam distance, providing insights into how desired steering effects can be achieved by choosing specific materials and tuning the effective LC birefringence with external stimuli like electric fields.

While we focused on light propagation in a plane orthogonal to the vortices, with the optical axis patterns also bound to this plane, our findings can be extended to more complex patterns of vortices, exceeding the insights related to analogies with cosmic strings. For example, in three dimensions the $\pi_1(\ ^2/\ _2) =\ _2$ LC vortices allow for confining twisted regions, with a refractive index seen by the extraordinary light higher than that of the surrounding medium (Extended Data Fig. 10), so that topological steering can also arise from wavopological 0 8.25 39k(o a.85040283 Tm (/)Tj 4.9nde)14.89999961(x s)10(een b)10(y th

33. Kleman, M. & Lavrentovich, O. D. *Soft Matter Physics: An Introduction* (Springer New York, 2003).
34. Sátiro, C. & Moraes, F. Lensing e□ects in a nematic liquid crystal with topological defects. *Eur. Phys. J. E* **20**, 173–178 (2006).
35. Figueiredo, D., Moraes, F., Fumeron, S. & Berche, B. Cosmology in the laboratory: an analogy between hyperbolic metamaterials and the Milne universe. *Phy. Rev. D* **96**, 105012 (2017).
36. Yeh, P. & Gu, C. *Optics of Liquid Crystal Displays* (John Wiley & Sons, 1999).
37. Liu, Q. et al. Plasmonic complex fluids of nematiclike and helicoidal self-assemblies of gold nanorods with a negative order parameter. *Phys. Rev. Lett.* **109**, 088301 (2012).
38. Lebach, D. E. et al. Measurement of the solar gravitational deflection of radio waves using very-long-baseline interferometry. *Phys. Rev. Lett.* **75**, 1439–1442 (1995).
39. Chang, K. & Refsdal, S. Flux variations of QSO 0957+561A,B and image splitting by stars near the light path. *Nature* **282**, 561–564 (1979).
40. Inada, N. et al. SDSS J1029+2623: a gravitationally lensed quasar with an image separation of 22.″5. *Astrophys. J.* **653**, L97 (2006).
41. Dhara, S. & Madhusudana, N. V. Physical characterisation of 4′-butyl-4-heptyl-bicyclohexyl-4-carbonitrile. *Phase Transit.* **81**, 561–569 (2008).
42. Li, J., Wu, S.-T., Brugioni, S., Meucci, R. & Faetti, S. Infrared refractive indices of liquid crystals. *J. Appl. Phys.* **97**, 073501 (2005).
43. Gauza, S., Wen, C. H., Wu, S.-T., Janarthanan, N. & Hsu, C. S.

Methods

Sample preparation

To fabricate LC cells, glass plates with or without transparent electrodes were spin-coated using 1.0 wt% azobenzene dye SD1 in dimethylformamide at 3,000 r.p.m. for 45 s and subsequently baked on a hotplate at 100 °C for 10 min to evaporate the residual solvent. Glass substrates with indium tin oxide coatings were used to fabricate cells for experiments involving application of electric fields[56–59]. To define the gap between the two confining glass plates, a fast-setting epoxy glue containing silica spacer spheres (15–60 μm in diameter, from Thermo Fisher) was placed near the corners of one glass plate (Fig. 2b and Extended Data Fig. 1a); the other glass plate was then lapped atop, leaving a small fraction of the electrode layer exposed for the connection to an external voltage supply (GFG-8216A, GW Instek). After the epoxy was fully solidified, a coverslip with a thickness of 0.17 mm was glued to the cell edge (Fig. 2b and Supplementary Notes), as needed for focusing a laser beam at the cell entry to launch a nematicon. The surface of the coverslip was pretreated with a polyvinyl alcohol (Dupont) film and mechanically rubbed using velvet cloth to impose strong and uniform boundary conditions[60]. The cell was then photo-patterned with a predesigned geometry for $\mathbf{n}(\mathbf{r})$ to induce the desired vortices via the method described in the following. After the photo-patterning, a commercial LC mixture E7 (Shijiazhuang Chengzhi Yonghua Display Material Co.) was filled into the empty cell by capillary forces at an elevated temperature of 100 °C and then quenched to room temperature under ambient conditions.

Photo-patterning of vortices

Our mesostructured LC vortices were architected by spatially orienting LC molecules on the inner surfaces of the two confining glass plates with an ~10-nm-thin layer of the azobenzene dye[61], a polarization-responsive photoalignment material. Upon being illuminated with a small dose (that is, ~200 mJ cm^{-2}) of linearly polarized blue light, the azobenzene moieties of the dye molecules orient orthogonally to the light's polarization direction, yielding robust surface boundary conditions[61] for the $\mathbf{n}(\mathbf{r})$ of the LC (Extended Data Fig. 1a). By using a LC microdisplay, all desired two-dimensional boundary condition geometries for $\mathbf{n}(\mathbf{r})$ can be predefined through spatially illuminating linearly polarized blue-light patterns, as controlled on a pixel-by-pixel basis with computer software. As schematically shown in Extended Data Fig. 1b, a blue-light pattern generated by computer is projected through the microdisplay with 1,024 × 768 pixels (EMP-730, Epson) and then relayed by three lenses to the back aperture of an objective. The blue light imprinting the pattern is focused on the azobenzene dye layers. The two azobenzene dye layers on the opposite inner surfaces of the confining glass plates can be patterned for boundary conditions sequentially or at the same time, depending on the cell gap relative to the focus depth of the objective[62]. I

from the given pattern of the LC alignment field, and the light path was calculated by forward Euler integration of equation (6). The light coming from a source at infinity was numerically prepared as parallel rays (Extended Data Fig. 2), and the deflection angle was determined by the total orientational change of d**r** until the ray reaches the observer colinear with the light source and cosmic string (Fig. 6c,d), or for large deflection at a radius from the pattern's centre (Extended Data Fig. 2). In other cases, the starting position and direction of rays were chosen to match those in our experimental images; an exponential decay in intensity of the light beam was artificially introduced for Fig. 4a,b to avoid the overlap of the trajectories and mimic interactions that do not preserve the solitonic nature of the beams upon their splitting. Light trajectories generated with this approach are shown as solid red lines, as an example, in Fig. 1b–f.

To account for the finite width of the optical solitons used in experiments, our modelling of ray trajectories based on the two approaches used multiple rays to numerically reveal effects like optical soliton fission. In this case, an appropriate alignment of the multi-ray numerical counterpart of the finite-width optical soliton relative to the half-integer vortices within the cores of a $k = 3$ vortex not only could reveal the fission itself, but also could reproduce the fine details of daughter soliton propagation and even the secondary fission of daughter solitons (Fig. 4).

In our numerical modelling, a linear optical soliton–vortex interaction is assumed, as in refs. [25,28,48,49]. Even though a nonlinear response of the LC is needed to fully describe the formation of nematicons, ray tracing in the linear optical regime sufficiently reproduces the

65. Smalyukh, I. I., Lansac, Y., Clark, N. A. & Trivedi, R. P. Three-dimensional structure and multistable optical switching of triple-twisted particle-like excitations in anisotropic fluids. *Nat. Mater.* **9**, 139–145 (2010).
66. Varney, M. C., Jenness, N. J. & Smalyukh, I. I. Geometrically unrestricted, topologically constrained control of liquid crystal defects using simultaneous holonomic magnetic and holographic optical manipulation. *Phys. Rev. E* **89**, 022505 (2014).
67. Piccardi, A., Alberucci, A. & Assanto, G. Nematicons and their electro-optic control: light localization and signal readdressing via reorientation in liquid crystals. *Int. J. Mol. Sci.* **14**, 19932–19950 (2013).
68. Izdebskaya, Y. V., Desyatnikov, A. S., Assanto, G. & Kivshar, Y. S. Deflection of nematicons through interaction with dielectric particles. *J. Opt. Soc. Am. B* **30**, 1432–1437 (2013).
69. Joets, A. & Ribotta, R. A geometrical model for the propagation of rays in an anisotropic inhomogeneous medium. *Opt. Commun.* **107**, 200–204 (1994).
70. Poy, G. & Žumer, S. Ray-based optical visualisation of complex birefringent structures including energy transport. *Soft Matter* **15**, 3659–3670 (2019).
71. Hiroyuki, M., Gartland, E. C., Kelly, J. R. & Bos, P. J. Multidimensional director modeling using the Q tensor representation in a liquid crystal cell and its application to the π cell with patterned electrodes. *Jpn. J. Appl. Phys.* **38**, 135–146 (1999).
72. Ravnik, M. & Žumer, S. Landau–de Gennes modelling of nematic liquid crystal colloids. *Liq. Cryst.* **36**, 1201–1214 (2009).
73. Mundoor, H., Wu, J.-S., Wensink, H. H. & Smalyukh, I. I. Thermally reconfigurable monoclinic nematic colloidal fluids. *Nature* **590**, 268–274 (2021).
74. Klus, B., Laudyn, U. A., Karpierz, M. A. & Sahraoui, B. All-optical measurement of elastic constants in nematic liquid crystals. *Opt. Express* **22**, 30257 (2014).
75.

https://doi.org/10.1038/s41563-022-01414-y

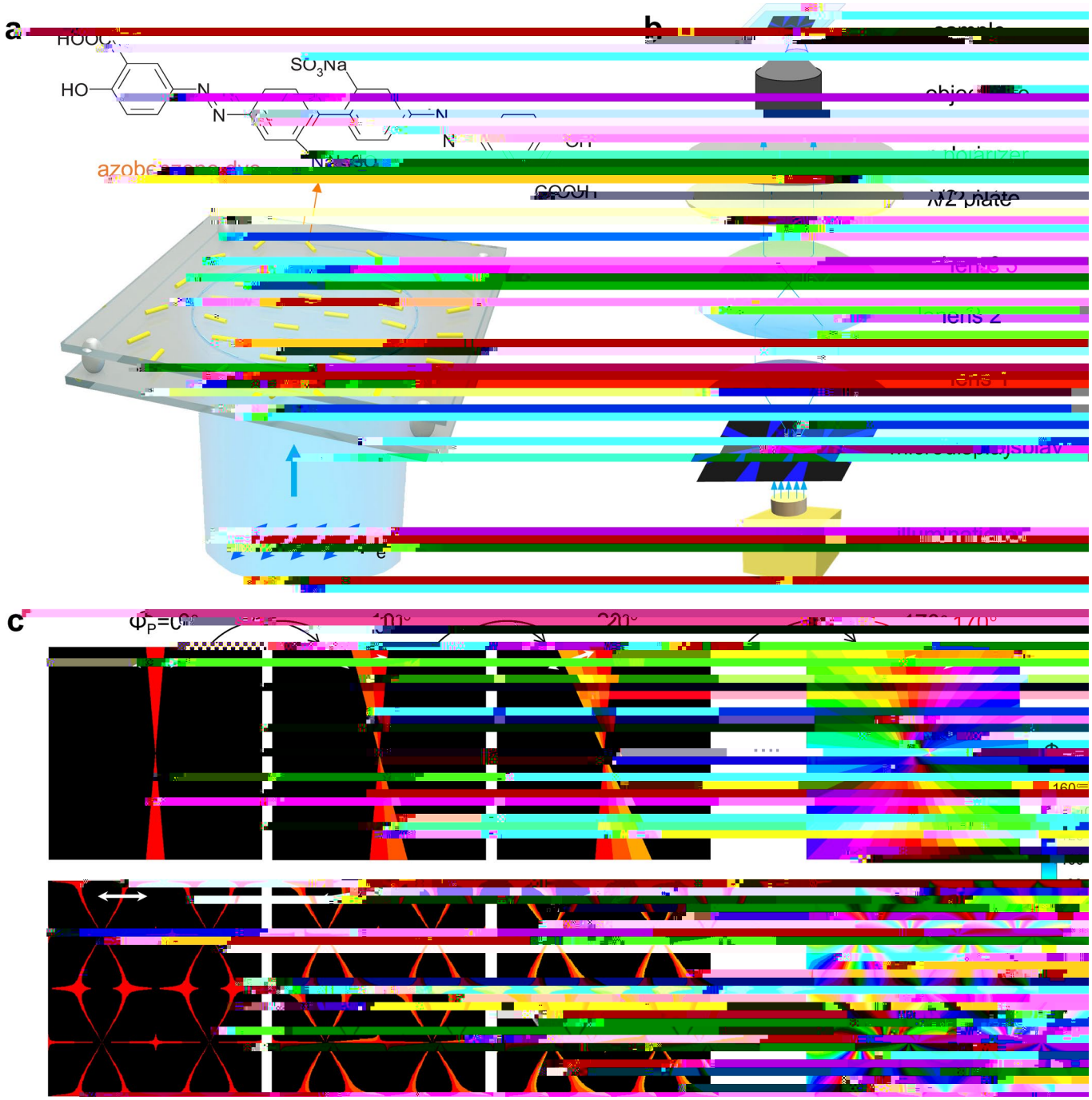

Extended Data Fig. 1 | Principles of photo-patterning of LC vortices. **a**, Optical response of azobenzene dye molecules to linearly polarized blue light, with the dye molecular structure shown above. When illuminated by the blue light, randomly oriented rodlike dye molecules collectively re-align to point orthogonally to the excitation light's polarization direction. **b**, Schematic setup of a custom-built photo-patterning system. The photo-patterning is based on a microdisplay used to project a computer-controlled blue-light pattern that is relayed by three lenses, linearly polarized by an inserted half-wave plate and a polarizer, and then projected to the back aperture of an objective, which focuses the pattern on the azobenzene dye layers. The pattern size is defined by the magnification of the objective. **c**, Vortices and their arrays are generated via sequential illuminations of patterns corresponding to narrow angular sectors of azimuthal orientations of dye molecules, synchronized with the corresponding control of the linear polarization (double white arrows) and its azimuthal orientation angle (Φ_p) to define dye molecule orientations at surfaces and, thus, define boundary conditions for $\mathbf{n}(\mathbf{r})$.

https://doi.org/10.1038/s41563-022-01414-y

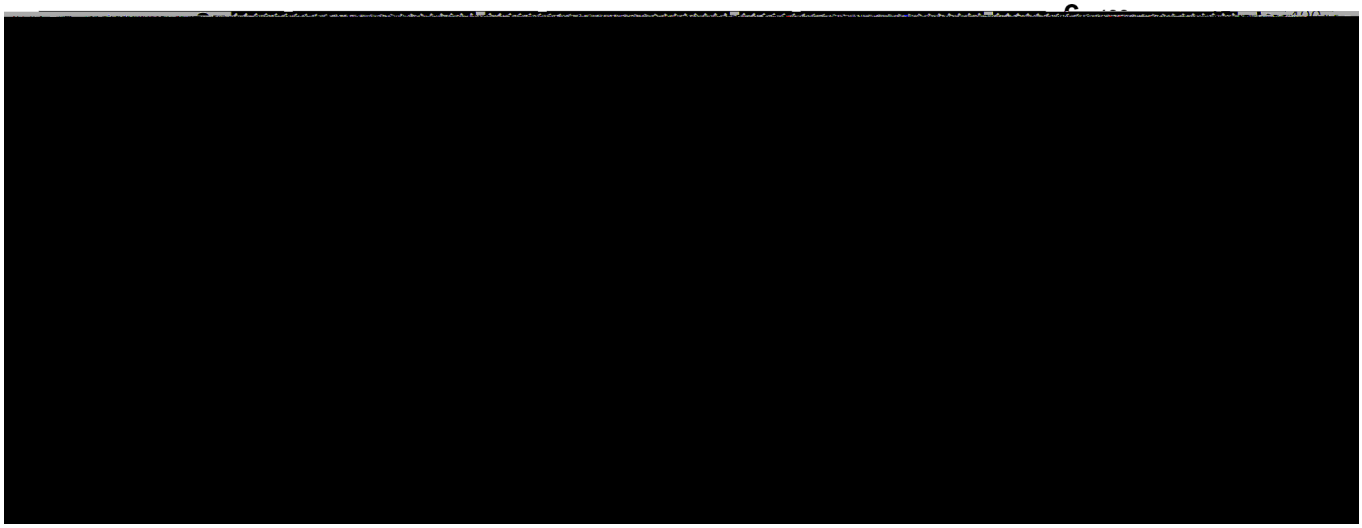

Extended Data Fig. 2 | Light steering in LCs with different Δ*n*. Numerically simulated optical trajectories (red/cyan lines) of light passing near the (**a**) $k = 1$, $\Psi_0 = \pi/2$ and (**b**) $k = 1$, $\Psi_0 = 0$ vortices formed within LCs with Δn of 0.015, 0.2, 0.8 and 1.7. The beams incident from the left side are initially parallel to the horizontal edges of the structures. White cylinders depict the spatial orientation of **n**(**r**). **c**, Numerically simulated deflection angle θ for such systems, with the value of θ being positive (negative) for deflection towards (away from) the center, as defined in the insets. Vertical dashed lines mark the material parameters for LCs including CCN-47 ($\Delta n = 0.015$), E7 ($\Delta n = 0.24$) and SHB-6 ($\Delta n = 0.79$). $n_o = 1.53$ for all simulations.

https://doi.org/10.1038/s41563-022-01414-y

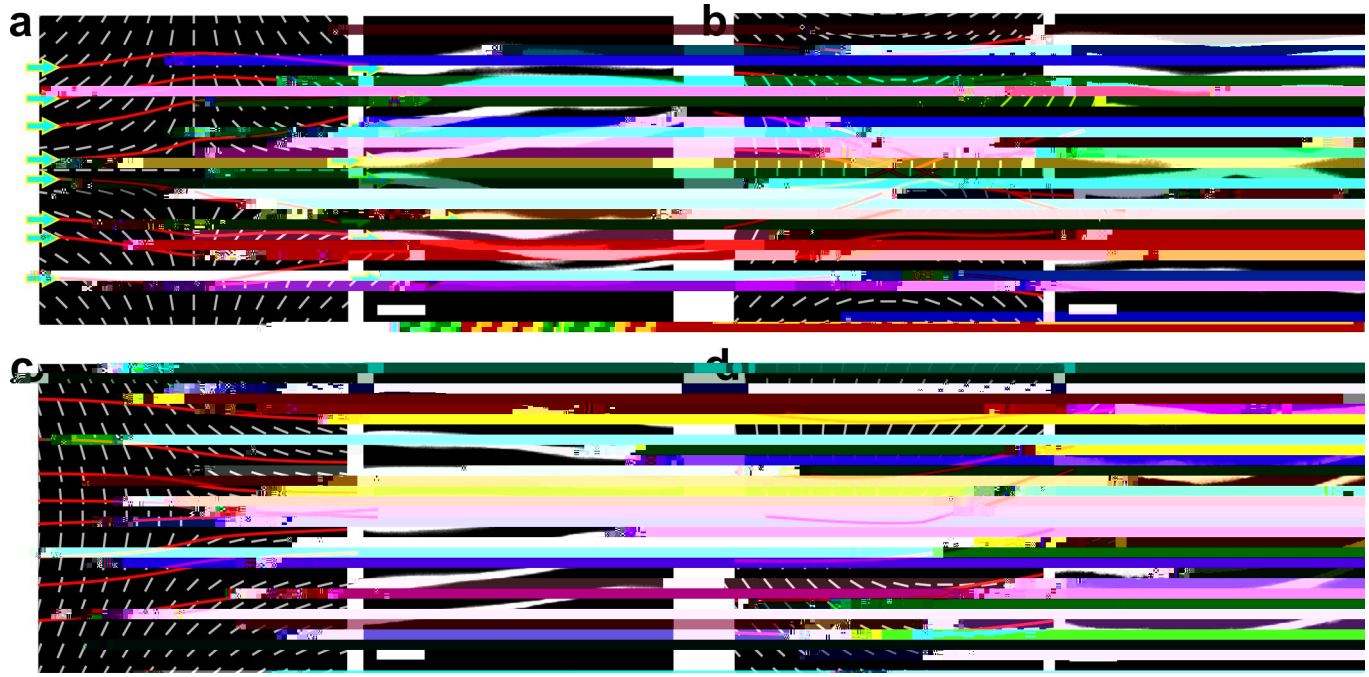

Extended Data Fig. 3 | Guiding of light by various topological vortices. **a-d**, (left) Computer-simulated light trajectories (red lines) overlaid atop of corresponding **n**(**r**) (white cylinders) and (right) experimental light propagation trajectories of 1064 nm laser beams emerging from different entry points (cyan arrows with yellow frame). The studied vortices from (**a**) to (**d**) are defects with: (**a**) $k = -1$, $\Psi_0 = 0$; (**b**) $k = -1$, $\Psi_0 = \pi/2$; (**c**) $k = -1/2$, $\Psi_0 = 0$ and (**d**) $k = 1/2$, $\Psi_0 = \pi/8$, respectively. The simulated beam trajectories are obtained using the Hamiltonian approach of ray tracing (Methods). All scale bars are 100 μm.

https://doi.org/10.1038/s41563-022-01414-y

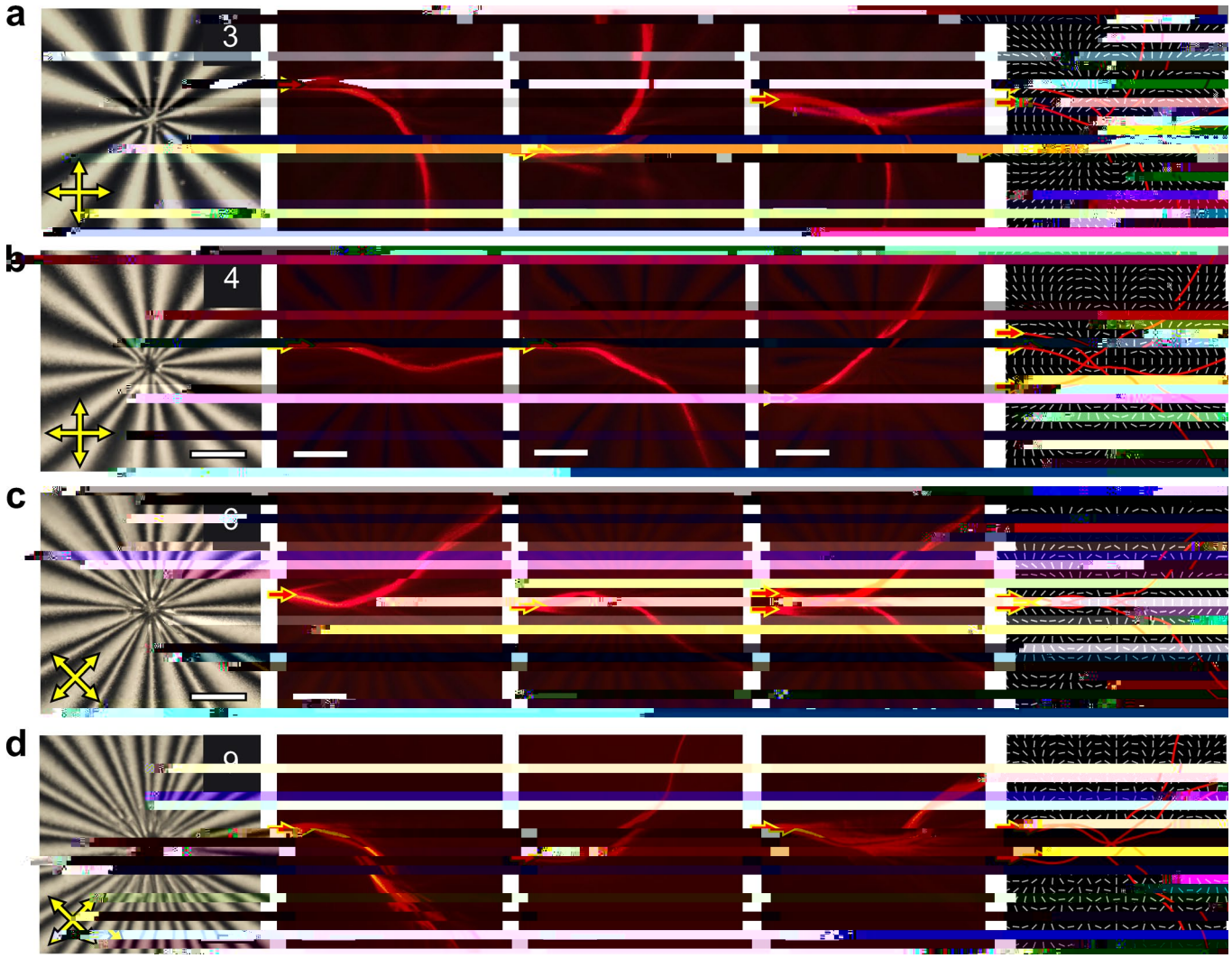

Extended Data Fig. 4 | Optical soliton steering by high-winding-number vortices. a-d, (left) Polarizing optical micrographs of vortices with winding numbers of k = 3, 4, 6 and 9 (marked on images) obtained between crossed polarizers (double yellow arrows). (3 middle panels) Experimental optical soliton trajectories for 650 nm laser beam launched at sites marked by red arrows with yellow frame, which closely match (right) computer-simulated trajectories plotted atop of associated **n**(**r**) (white cylinders). All scale bars are 100 µm.

https://doi.org/10.1038/s41563-022-01414-y

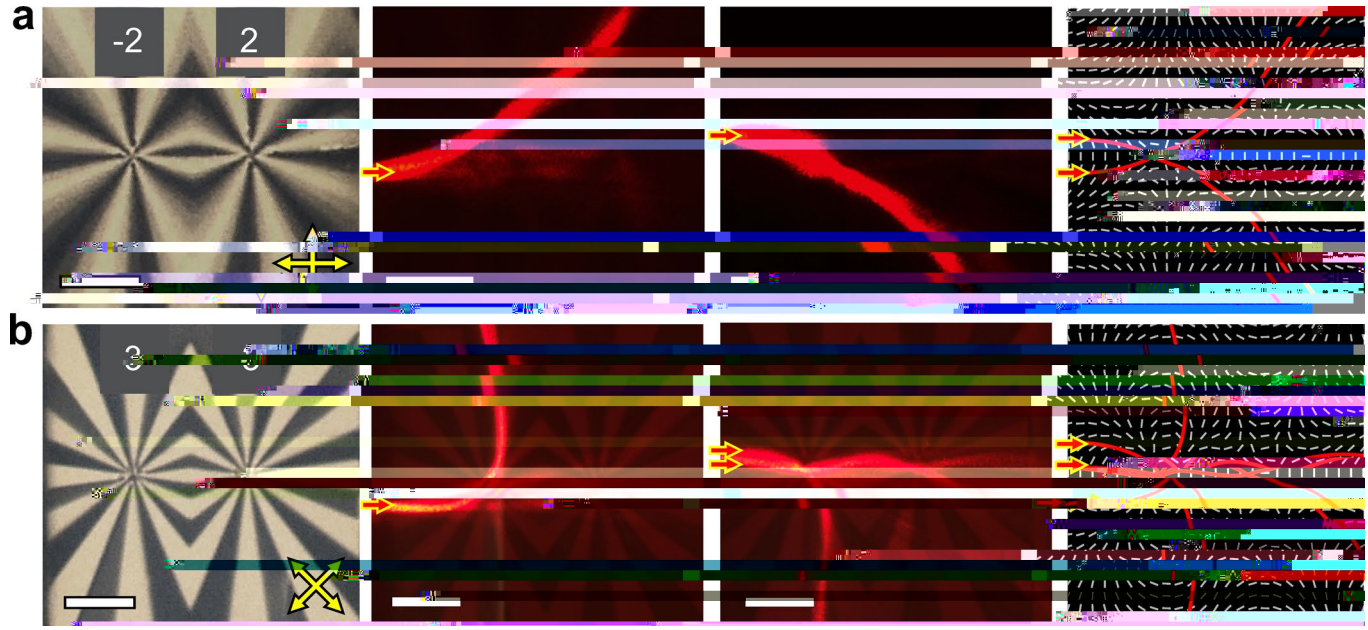

Extended Data Fig. 5 | Optical soliton steering by topological vortex dimers. **a-b**, (left) Polarizing optical micrographs of vortex dimers formed by vortices with (**a**) $k = -2$ and $k = 2$ and (**b**) $k = 3$ and $k = -3$, obtained under crossed polarizers (double yellow arrows). (2 middle panels) Optical soliton trajectories of 650 nm laser beam closely match (right) computer-simulated trajectories shown atop of the associated **n**(**r**) (white cylinders). All scale bars are 200 μm.

https://doi.org/10.1038/s41563-022-01414-y

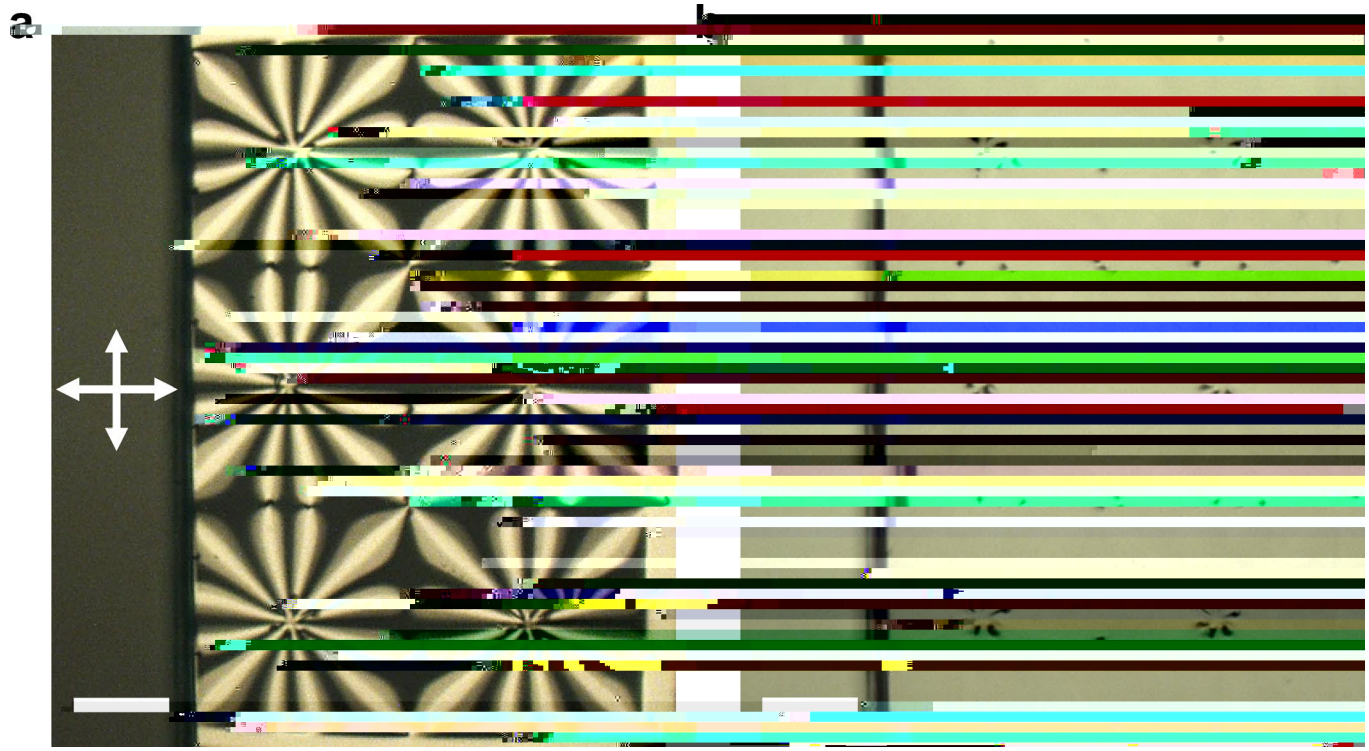

Extended Data Fig. 6 | Optical characterization of a vortex array. **a**-**b**, Polarizing (**a**) and brightfield (**b**) optical micrographs of a 3×2 array containing a vortex with $k = 3$, $\Psi_0 = 0$ surrounded by 12 bright and 12 dark brushes corresponding to 6π azimuthal **n**(**r**)-rotation in (**a**). The dark spots in (**b**) are half-integer defects to which cores of $k = 3$ (hexagons of dark spots) and $k = -1$ (pairs of dark spots) vortices split. Double white arrows mark orientations of crossed polarizers. Both scale bars are 200 μm.

https://doi.org/10.1038/s41563-022-01414-y

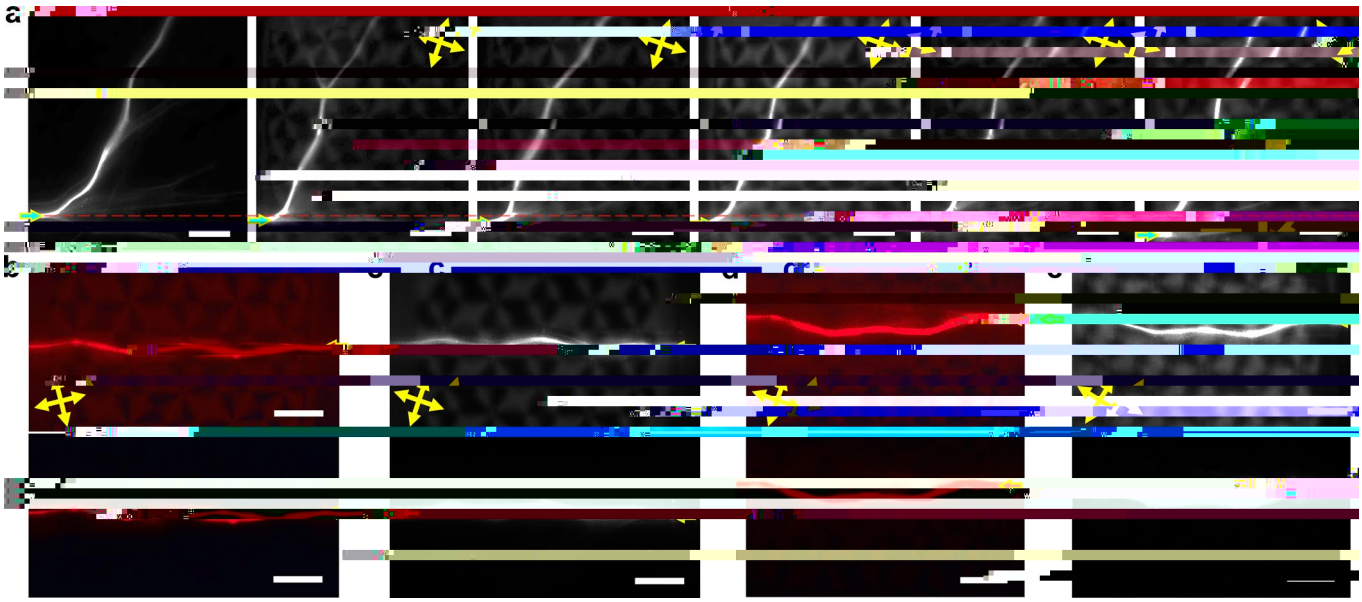

Extended Data Fig. 7 | Optical soliton propagation within arrays with $k = 1$ vortices. a, Lightning-like optical soliton propagations after slightly shifting 1064 nm laser beam with respect to the array. **b**-**e**, Meandering solitonic light trajectories generated by 650 nm (**b**,**d**) and 1064 nm (**c**,**e**) laser beams. The trajectories are captured (upper) with and (lower) without illumination backlight of the microscope. Double yellow arrows mark orientations of crossed polarizers. All scale bars are 200 μm.

https://doi.org/10.1038/s41563-022-01414-y

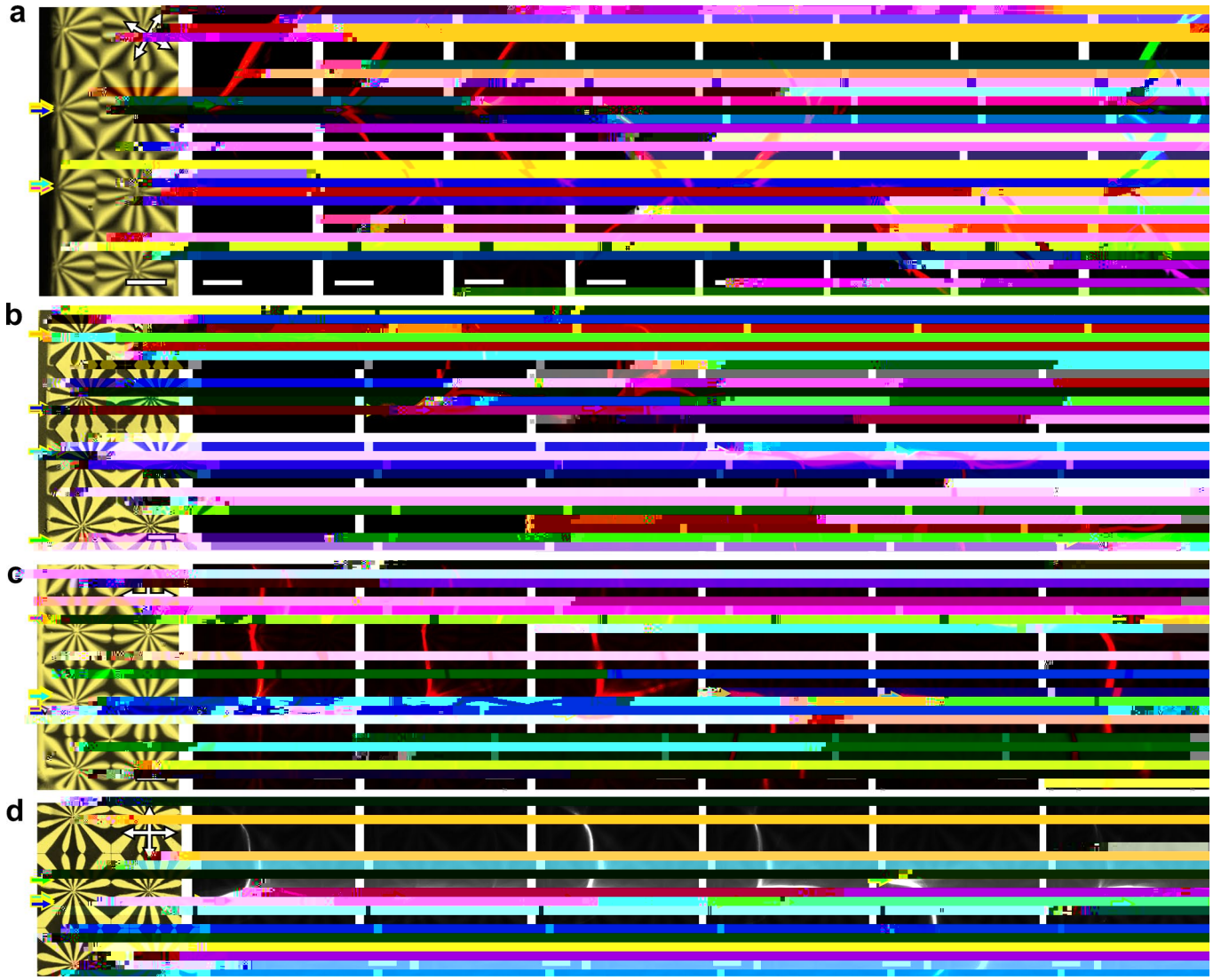

Extended Data Fig. 8 | Controlled fission of optical solitons. a-d, Interaction of light beams with arrays containing (**a**) $k = 3$, $\Psi_0 = \pi/2$ vortices and (**b-d**) $k = 3$, $\Psi_0 = 0$ vortices: (left panels) polarizing optical micrographs and (other panels) the corresponding experimental beam trajectories. Rightmost panel in (**a**) shows superposition of the individual light trajectories distinguished by false colours. All different soliton trajectories and fission events are obtained by slight shifting of the launching site of the beam, as marked by colored arrows with yellow frame. All scale bars are 200 µm, showing dimensions of the studied vors with yelloaysion e. The Al sa T* [(All sa3.800g°-10.64099997 slo)146999998(wing dimensions o)4.8000002(f the

https://doi.org/10.1038/s41563-022-01414-y

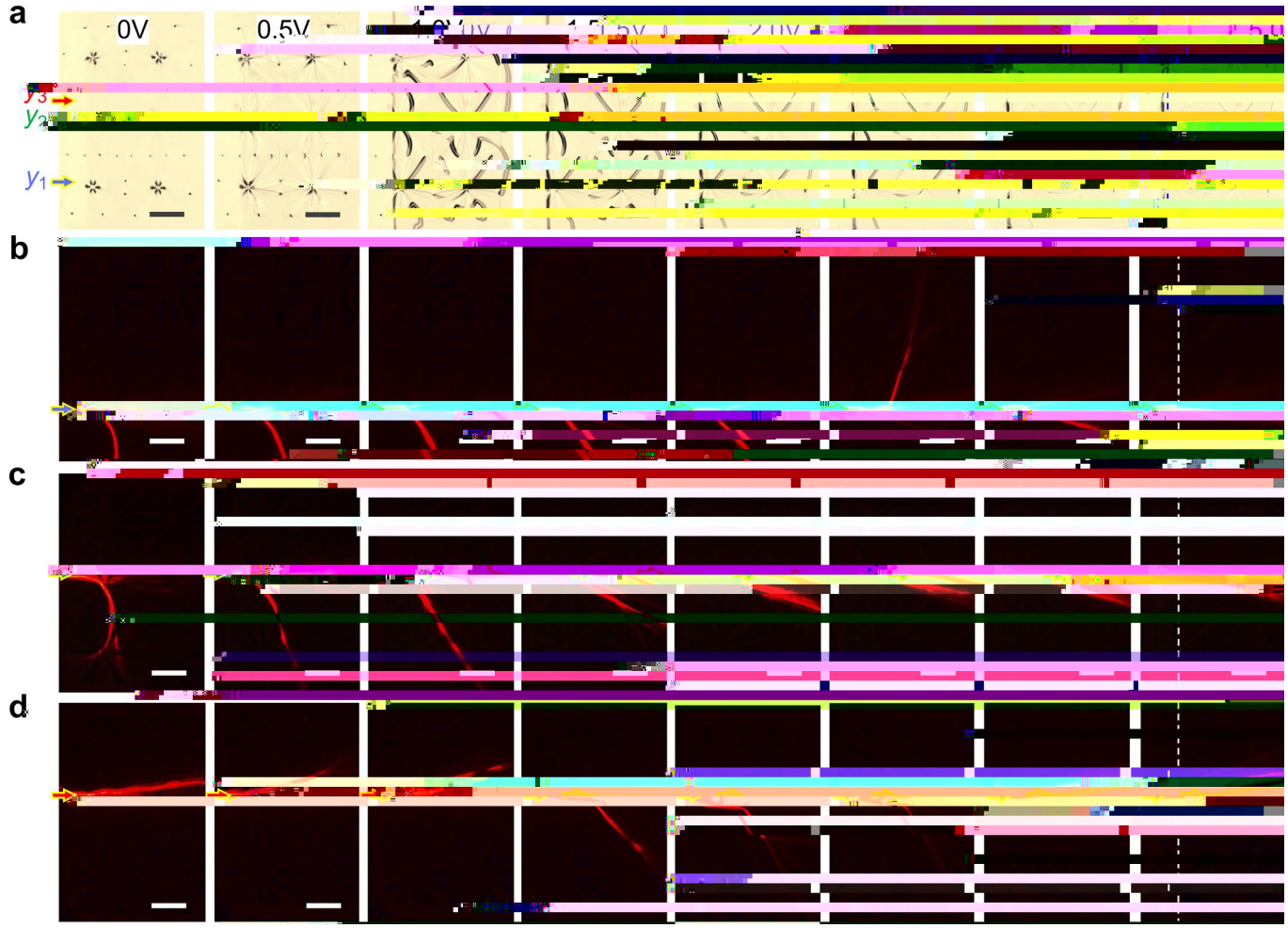

Extended Data Fig. 9 | Electric control of topological steering by an array with $k = 3$ vortices. a, Evolution of brightfield micrographs when applied voltage increases from 0 to 5.0 V, as marked on images. **b-d**, Light deflection trajectories at voltages corresponding to (**a**) when beams are launched from positions y_1, y_2 and y_3 marked in (**a**). Blue (**a**) and white (**b-d**) dashed lines mark the edge of indium tin oxide electrodes, with the right-side of the sample having the electrode and being responsive to applied voltage. All scale bars are 200 µm.

https://doi.org/10.1038/s41563-022-01414-y

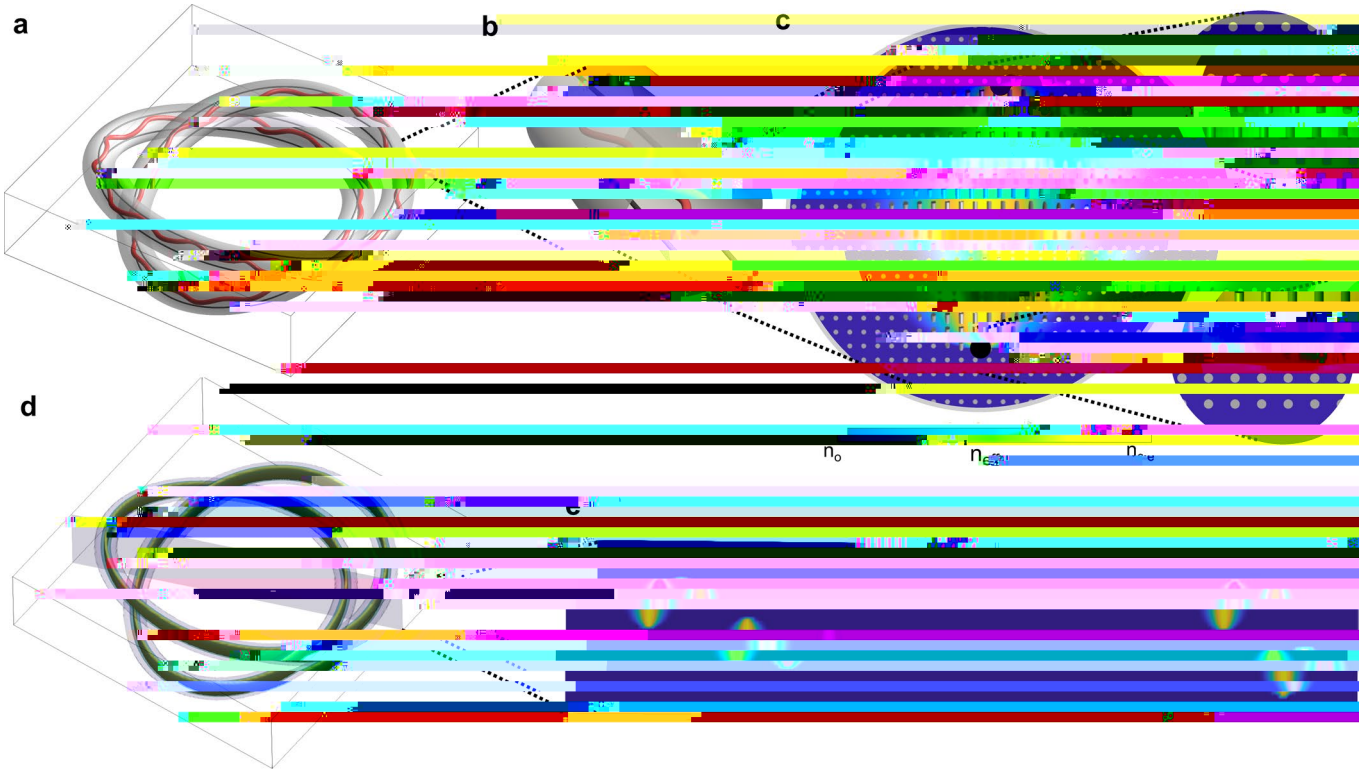

Extended Data Fig. 10 | Engineering knots of light beams with the help of knotted vortices. a, Waveguiding of a light beam (red line) in a high-index knotted region defined by a pair of trefoil-knot-shaped loops of vortices (black lines). **b**, A zoom-in view of the tube-like high-index region forming the trefoil knot shown in (**a**). **c**, A detailed view of the director structure and refractive index distribution within a cross-section of the knotted tubelike region, where the right-side insets show details of director rotations around the vortex lines and the bottom inset provides the colour scheme for the refractive index varying between the ordinary and extraordinary values. **d**, The three-dimensional distribution of the refractive index variation and **e**, its corresponding variation in a cross-sectional plane depicted in (**d**), with the high-index regions corresponding to intersections of the knotlike high-index structure with the plane, as clearly seen. Once coupled to such a knot-shaped topological waveguide, light would be confined to propagate within the knot.